RSC Advances

This article can be cited before page numbers have been issued, to do this please use: X. Zhang, Z. Pei, H. Lu and H. Huang, *RSC Adv.*, 2016, DOI: 10.1039/C6RA14699F.

ROYAL SOCIETY OF CHEMISTRY

www.rsc.org/advances

View Article Online
DOI: 10.1039/C6RA14699F

RSC Advances

ARTICLE

Morphology-dependent Properties of CeO_2 Nano-catalysts on CH_2Cl_2 Oxidation

Received 00th January 20xx,
Accepted 00th January 20xx

DOI: 10.1039/x0xx00000x

www.rsc.org/

Xinhua Zhang, [a, b] Zhiying Pei, [a] Hanfeng Lu [c] and Haifeng Huang [a,*]

Four types of CeO_2 nanoparticles with different morphologies (nanorods, nanocubes, nanopolyhedra, and bulk CeO_2 nanoparticles) were synthesized and used in dichloromethane (DCM) oxidation. Their detailed physicochemical properties were investigated by X-ray diffraction, N_2 physisorption, H_2 temperature-programmed reduction, high-resolution transmission electron microscopy, and X-ray photoelectron spectroscopy. Results indicated that DCM oxidation over CeO_2 nanoparticles has significant morphology-dependent effects. CeO_2 nanorods showed the best activity among all the investigated samples (T_{90} is only 323 °C). The main products were CO_2 and HCl, although trace amounts of $CHCl_3$, CCl_4, CO, and Cl_2 could be detected. The high performance of CeO_2 nanorods in DCM oxidation may be related to the abundant surface defects, increased amount of adsorbed active oxygen species, and good reducibility of the catalyst.

1 Introduction

The chlorinated volatile organic compounds (CVOCs) emitted by numerous industries are highly toxic, carcinogenic, and genotoxic to humans, even at very low concentrations [1]. Thus, various countries set stringent emission ceilings to these harmful compounds. In addition, several abatement techniques have been developed to meet the increasingly strict legislations. Catalytic combustion is one of the most promising approaches to destroy CVOCs because it can be operated at a relatively low temperature range as compared with the thermal incineration process [2]. The formation of NO_x can also be restrained.

Undoubtedly, the catalyst is a key factor in CVOC oxidation. A suitable catalyst is highly active for the target CVOCs and should have good selectivity for the desired products (CO_2 and HCl). Supported noble metals [3-5], transition metal oxides [2, 6], and zeolites [7, 8] are usually reported in CVOC oxidation. Supported noble metal catalysts show relatively higher activity than the other two counterparts in a low-temperature range but are easily poisoned by chlorinated intermediates from CVOC destruction [9, 10]. Although the transition metal oxides are less active than the supported noble metals in most cases, these catalysts are believed to be more resistant to chlorine poisoning [2, 11]. Notably, transition metal oxides are also more abundant and much cheaper than noble metals. Therefore, the use of transition metal oxides to substitute noble metals in CVOCs oxidation is highly significant. However, their activity in the low-temperature range still needs to be resolved.

CeO_2-based catalysts have been extensively studied in CVOC oxidation for their unique redox properties and high C–Cl bond dissociation ability [2, 12-15]. However, the strong adsorption of chloride species on the surface of CeO_2 during CVOC destruction will cause the partial deactivation of the catalysts [12, 15]. A conventional approach to resolve this problem is to incorporate CeO_2 with other transition metal oxides [2, 13-15]. However, deactivation could be still observed. Recently, CeO_2 nanoparticles with anisotropic shapes at the nanometer scale have attracted much interest. These materials can significantly improve the reaction performance when their specific facets are selectively exposed [16-19]. The morphology effects of ceria nanoparticles have been identified in CO [20-22] oxidation and the WGS reaction [23, 24]. However, the morphology-dependent properties of CeO_2 in CVOC oxidation have not been fully studied, although this oxide is widely used as catalyst in CVOC destruction. Herein, three types of low-dimensional CeO_2 nanoparticles (nanorods, nanocubes, and nanopolyhedra) were synthesized by a facile hydrothermal method and used in dichloromethane (DCM) oxidation. This study aimed to explore the structure–activity relationship of CeO_2 nano-catalysts during DCM oxidation.

2 Experimental

2.1 Catalyst preparation

Cerium (III) nitrate hexahydrate ($Ce(NO_3)_3{\cdot}6H_2O$), sodium hydroxide (NaOH), and DCM were analytical grade reagents. All chemicals were purchased from Aladin Reagents and used as received without further purification. The synthesis of CeO_2 nanorods and nanocubes followed the revised procedure of Mai et al [25]. Typically, $Ce(NO_3)_3{\cdot}6H_2O$ (3.4720 g) and NaOH (33.6 g) were dissolved in 20 mL and 140 mL of deionized water, respectively. The two solutions were subsequently mixed in a Teflon bottle, and the mixed solution was stirred for 30 min at room temperature to form a slurry. The Teflon bottle

[a] College of Biological and Environmental technology, Zhe Jiang University of Technology, Hang Zhou 310032, PR China.
[b] College of Chemical and Environmental engineering, Jiu Jiang University, Jiu Jiang 332005, PR China.
[c] College of Chemical Engineering, Zhe Jiang University of Technology, Hang Zhou 310032, PR China.
† Corresponding Author: Haifeng Huang; Email Address: hhf66@zjut.edu.cn; Tel: +86-571-88320385

View Article Online
DOI: 10.1039/C6RA14699F

was tightly sealed and placed in a stainless-steel autoclave. The tightly sealed autoclave was hydrothermally treated at 100 °C for 24 h. After cooling, the obtained white precipitates were collected by centrifugation, washed with deionized water for 3–4 times, and dried at 60 °C in air overnight. The acquired yellow powder was calcined in air at 450 °C for 5 h in a muffle furnace to obtain the CeO_2 nanorods. The synthesis of CeO_2 nanocubes was similar to that of CeO_2 nanorods, except the hydrothermal treatment temperature was set to 180 °C. The synthesis of CeO_2 nanopolyhedra mainly followed the procedure of Si et al [24], but the calcination temperature was revised to 450 °C. Typically, $Ce(NO_3)_3{\cdot}6H_2O$ (3.2567 g) was dissolved in 150 mL of NaOH solution (0.1 M). The mixture was stirred for 10 min at room temperature and transferred into a Teflon-lined stainless-steel autoclave. The autoclave was tightly sealed and hydrothermally treated at 180 °C for 24 h. The subsequent steps were followed to produce CeO_2 nanorods. For comparison, bulk CeO_2 nanoparticles were also prepared by directly calcinating $Ce(NO_3)_3{\cdot}6H_2O$ in air at 450 °C for 5 h. For convenience, the CeO_2 nanorods, nanocubes, nanopolyhedra, and bulk nanoparticles were denoted as CeO_2-r, CeO_2-c, CeO_2-p, and CeO_2-b, respectively.

2.2 Catalyst characterization

Powder X-ray diffraction patterns (XRD) were obtained on an X'Pert Pro powder diffract meter with the scanning rate of 0.1° per minute, using Cu Ka radiation (λ= 0.154056 nm). The phase compositions were analyzed using jade 6.5.

N_2-physical adsorption and desorption were recorded on Micromeritics ASAP 2020 at 77 K. The specific surface area of the samples was calculated from adsorption isotherms using the BET equation.

H_2 temperature-programmed reduction (H_2-TPR) was measured on FINE SORB-3010 E instrument equipped with a thermal conductivity detector (TCD). 200 mg of sample was heated from 50 to 900 °C in a 10 vol% H_2/Ar flow (30 mL min^{-1}) at a ramp of 10 °C/min.

High Resolution Transmission Electron Microscope (HR-TEM) images of the samples were obtained using Philips-FEI (Tecnai G2 F30 S-Twin). All samples were ultrasonically dispersed in absolute alcohol for 1 h, then the suspension was deposited on an amorphous carbon-coated circular copper grid before measurement.

X-ray photoelectron spectroscopy (XPS) spectra of the samples were recorded on a Kratos AXIS Ultra DLD photoelectron spectrometer (Shimadzu scientific instruments, Japan) and using a monochromatic radiation source Al K (45 W, 3×10^{-9} mbar). The charging of samples was corrected by setting the binding energy (BE) of adventitious carbon (C 1s) at 284.8 eV.

Laser Raman spectra were obtained on LabRAM HR-800 spectrometer (Horiba Jobin Yvon, France) equipped with an air-cooled multichannel CCD detector, Ar^+ ion (531.95) was employed as an excitation source (Nd: YAG 20 mW) to obtain visible Raman spectra.

2.3 Activity test

DCM oxidation experiments were conducted in a fixed bed tubular reactor (6 mm i.d.) under atmosphere pressure between 150 °C and 450 °C. 200 mg catalysts (40-60 mesh) was loaded in the center of the reactor and sandwiched with quartz wool. 1.8 g of quartz sand was placed on the inlet-end to preheat the feed gas. DCM feed concentration was kept constant at 1000 ppm by controlling the flow rate of bubbling air (20.8% O_2 and 79.2% N_2) through an ice bathed saturator, and the gas hourly space velocity (GHSV) in the reactor bed was set to 15000 mL g^{-1} h^{-1} by adjusting the flow rate of balance air in all experiments. The effluent gases were analyzed online with a GC-1620 gas chromatograph equipped with a flame ionization detector (FID) and a TCD. A further detailed analytic process was described in our previous work [6].

3 Results and discussion

3.1 Catalytic activity results

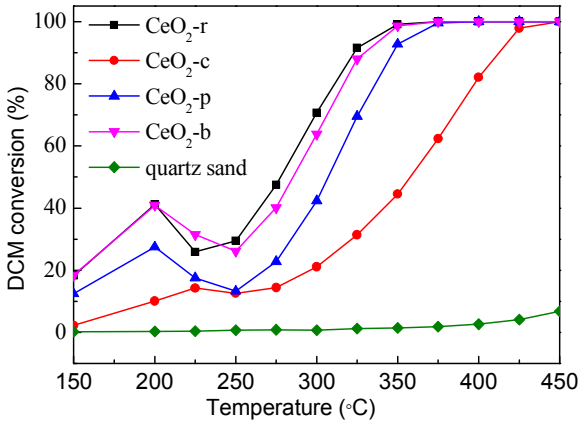

Fig. 1 Light-off curves of DCM over CeO_2 with different morphologies (1000 ppm DCM，air balance, GHSV: 15000 mL · g_{cat}^{-1} · h^{-1})

Fig. 1 shows the DCM conversion over CeO_2 nanoparticles with different morphologies. The pure quartz sand had almost no catalytic activity under the given testing conditions. The complete conversion of DCM could be achieved at 350–450 °C for all investigated samples. The values of T_{50} and T_{90} (temperatures with 50% and 90% DCM conversion achieved, respectively) are listed in Table 1. At T_{90}, the activity of the investigated samples was CeO_2-r > CeO_2-b > CeO_2-p > CeO_2-c. The CeO_2 nanorods showed the best activity; its T_{50} and T_{90} were only 278 and 323 °C, respectively. By contrast, the CeO_2 nanocubes showed the worst activity. Compared with the CeO_2 nanorods, the T_{50} and T_{90} of CeO_2 nanocubes increased 81 and 90 °C, respectively. DCM oxidation showed the different activities of CeO_2 nanoparticles with different morphologies.

Fig. 1 also shows that DCM conversion experienced temporary deactivation in the temperature range of 200–250 °C, which could be attributed to the chlorine species adsorption on the catalyst's active sites in relative low temperature range during DCM destruction. Similar phenomena were also observed by Dai et al

View Article Online
DOI: 10.1039/C6RA14699F

[26]. However, the gradual removal of Cl adsorption on the oxygen vacancies would be done thanks to the elevated temperature and high ratio of O/Cl in the feed gas [11]. Consequently, the activity of ceria was gradually recovered as the temperature increased.

The desired products of DCM oxidation are CO_2 and HCl. However, the poor selectivity may produce more toxic by-products. The main products of DCM oxidation over the investigated samples are CO_2 and HCl, with a small amount of trichloromethane (TCM), carbon tetrachloride (CCl_4), CO, and Cl_2, depending on the catalysts used.

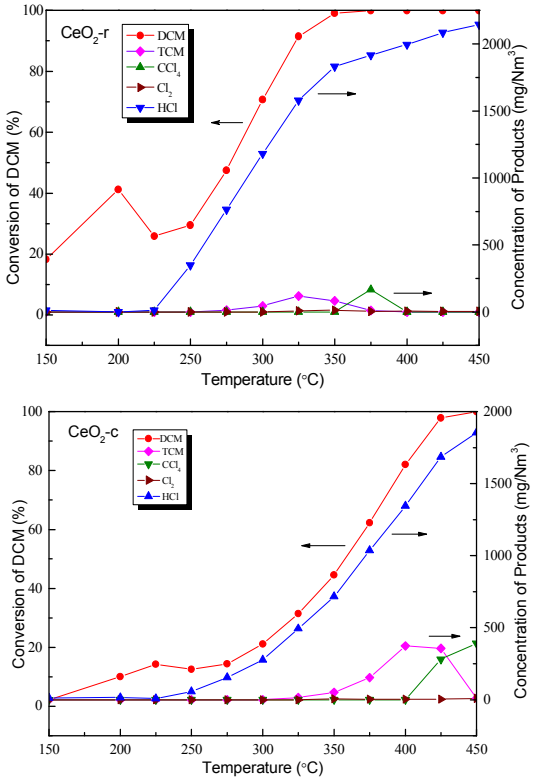

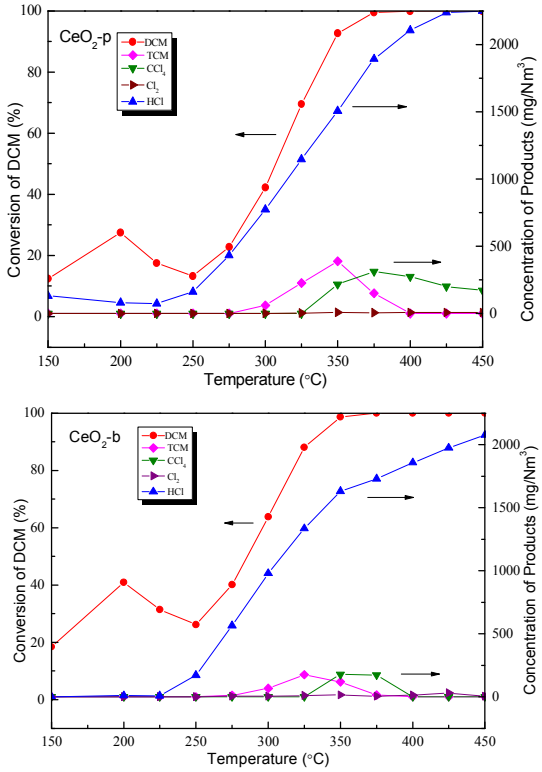

Fig.2 Selectivity of chlorinated species during DCM oxidation over CeO_2 with different morphologies (1000 ppm DCM, air balance, GHSV: 15000 mL · g_{cat}^{-1} · h^{-1})

Fig. 2 shows the selectivity of chlorinated species during DCM destruction. The maximum selectivity of HCl over CeO_2-r, CeO_2-c, CeO_2-p, and CeO_2-b was 65.46%, 56.61%, 72.56%, and 66.22%, respectively. For TCM, the order of maximum selectivity was CeO_2-p (350 °C) > CeO_2-c (400 °C) > CeO_2-b (350 °C) > CeO_2-r (325 °C). (Henceforth, the numbers in brackets indicate the corresponding temperature.) For CCl_4, the order of maximum selectivity was CeO_2-p (375 °C) > CeO_2-c (425 °C) > CeO_2-b (350 °C) > CeO_2-r (375 °C). CeO_2-r showed the worst selectivity for TCM and CCl_4, with the maximum concentrations of 118 and 116 mg/Nm^3, respectively; its selectivity was much less than when CeO_2-p was used as a catalyst (the maximum selectivity of TCM and CCl_4 was 374 and 390 mg/Nm^3, respectively). Meanwhile, a small amount of Cl_2 was also detected on all the investigated samples in the high-temperature range (above 300 °C), which could be related to the Deacon reaction ($2HCl + 1/2O_2 = H_2O + Cl_2$) [26, 27].

Table 1 Textual properties and activity data of the investigated samples

Samples	Crystallite Sizes ①/nm	BET area /m^2 g^{-1}	Total pore volume /cm^3 g^{-1}	Pore sizes /nm	T_{50}/T_{90} /°C	H_2 consumption② /umol g^{-1}	I_D/I_{F2g}
CeO_2-r	10.3	86.4	0.33	15.3	278/323	722	0.058
CeO_2-c	40.9	20.5	0.15	29.3	359/413	74	0.023
CeO_2-p	12.9	68.0	0.10	6.1	308/346	413	0.033
CeO_2-b	12.9	67.6	0.23	13.8	286/331	495	0.036

① The value were estimated by Scherrer equation, applied to the (1 1 1) reflection of CeO_2.

② The values were calculated from the reduction of standard CuO.

View Article Online
DOI: 10.1039/C6RA14699F

RSC Advances

ARTICLE

3.2 X-ray diffraction

The X-ray diffraction patterns of as-prepared samples are shown in Fig. 3, and the corresponding crystallite sizes are listed in Table 1. The diffraction peaks in 28.5°, 33.1°, 56.3°, and 59.1° can be clearly observed on all testing samples, which could be indexed to the cubic fluorite CeO_2 crystal phase (PDF# 89-8436, space group: Fm-3m). The diffraction peaks of CeO_2-c were much narrower than those of other samples, which was consistent with the larger crystallite sizes of this sample, as listed in Table 1. The results were also consistent with those of high-resolution transmission electron microscopy (HR-TEM) characterization (see below).

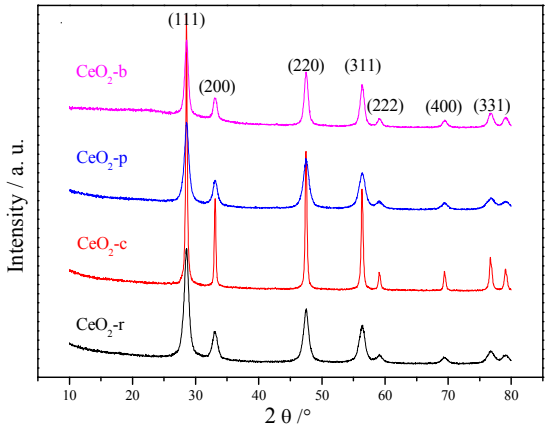

Fig. 3 The XRD patterns of investigated samples

3.3 N_2 physisorption by the Brunauer–Emmett–Teller method

The Brunauer–Emmett–Teller (BET) areas and corresponding pore volume and pore sizes of the investigated samples are listed in Table 1. CeO_2-r and CeO_2-c have the largest and smallest BET area as well as the best and worst activity during DCM oxidation, respectively. However, the activity of CeO_2-p was much inferior to that of CeO_2-b, although their BET areas were relatively comparable. These discrepancies could be also observed between the pore volume, pore sizes, and their activity in DCM oxidation. Therefore, the BET areas, pore volume, and pore sizes of nano-CeO_2 are not key factors of DCM oxidation. Other reasons may influence the activities of CeO_2 nanoparticles with different morphologies.

3.4 H_2 temperature-programmed reduction

The H_2 temperature-programmed reduction (H_2-TPR) of investigated samples is shown in Fig. 4. All tested samples displayed two or more reduction peaks involved different positions and relative intensities in the temperature range of 50–900 °C. Three main reduction peaks could be identified in the temperature range of 300-450 °C (α), 450-700 °C (β), and >700 °C (γ), respectively. The low-temperature reduction peak α involved a stepwise surface reduction process with the formation of nonstoichiometric CeO_{2-x} phase and oxygen vacancies in the surface layer [28]. These reduced oxygen species are usually attributed to the chemical adsorbed oxygen on the vacancies of CeO_2 [22]. For peak β, characterized with some connected reduction peaks, usually involved the reduction of subsurface layer and deep interior of CeO_2 nanoparticles [28]. The more complex reduction profiles of CeO_2-c, CeO_2-p and CeO_2-b indicate some kind of structural inhomogeneities of these samples as revealed in the next TEM characterizations. The peak γ at the high-temperature range (ca. 800 °C) is attributed to the reduction of bulk lattice oxygen anions of CeO_2 [12, 29]. It should be mentioned that the initial reduction temperature of capping oxygen ions was changed with the testing samples: CeO_2-r (145 °C) < CeO_2-b (154 °C) < CeO_2-p (168 °C) < CeO_2-c (173 °C), thereby indicating that the morphologies of CeO_2 influenced the activity of capping oxygen. The H_2 consumption of the investigated samples in the low-temperature range was calculated; the results are listed in Table 1. The order of H_2 consumption was CeO_2-r > CeO_2-b > CeO_2-p > CeO_2-c, which is mainly consistent with their activity in DCM oxidation (Fig. 1).

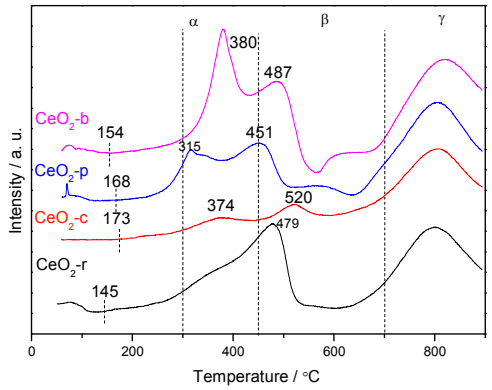

Fig. 4 H_2-TPR of investigated samples

3.5 HR-TEM

HR-TEM micrographs of the as-prepared samples are shown in Fig. 5. The morphologies of nanorods, nanocubes, and nanopolyhedra can be clearly observed, which are consistent with the experimental designs. The CeO_2-b nanoparticles were severely aggregated but no specific shapes were exhibited. Fig. 5a shows that the CeO_2 nanorods have a diameter distribution of 6–7 nm and a length distribution of 40–65 nm; their surfaces are rich in micropores. Fast Fourier-transform (FFT) revealed that the growth of CeO_2 nanorods are oriented in the [1 1 0] direction to expose the {1 1 0} and {1 1 1} planes (Fig. 5b). The CeO_2 nanocubes had a less uniform size distribution, with side lengths ranging from 50 nm to 100 nm, but all were cubic in shape (Fig. 5c). FFT revealed that this sample had selectively exposed {1 0 0} and {1 1 0} planes (Fig. 5d). The CeO_2 nanopolyhedra had a size distribution of 10–12 nm and selectively exposed {1 1 1} planes (Figs. 5e and 5f, respectively). Similar results were reported in [17, 24, 25]. Micrographs showed that the CeO_2 nanocubes had the

View Article Online
DOI: 10.1039/C6RA14699F

largest sizes, which is consistent with their having the smallest BET area and narrowest XRD peaks, as revealed in Table 1 and Fig. 3, respectively.

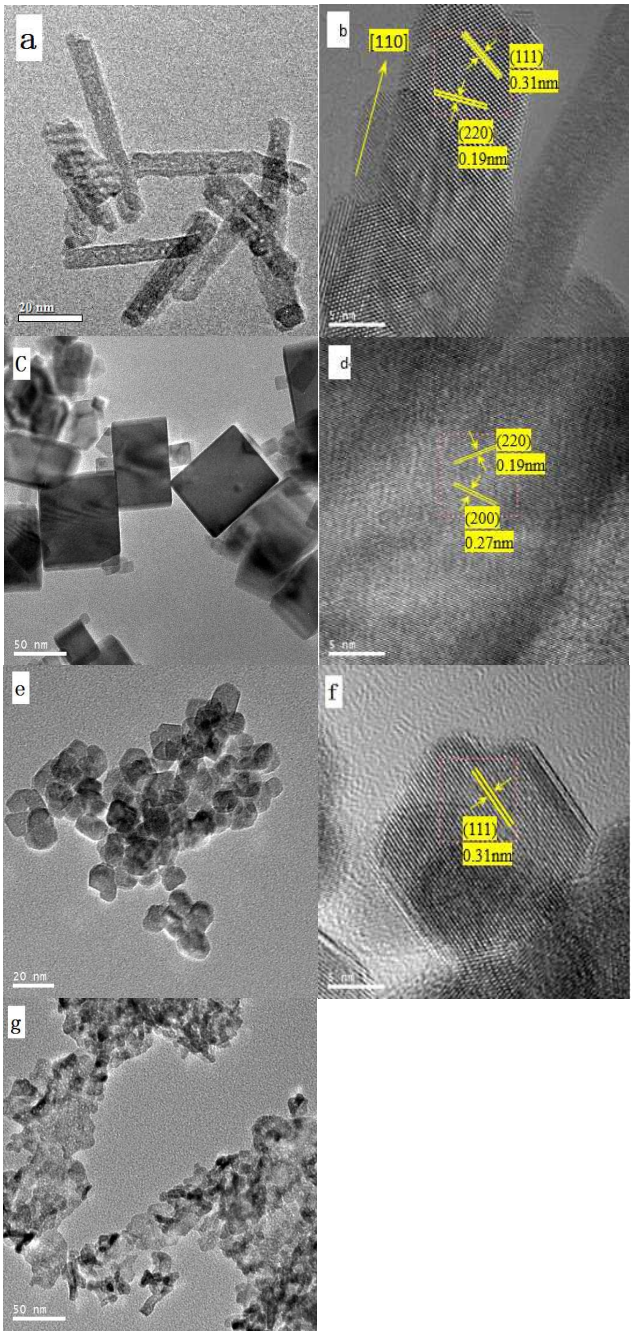

Fig. 5 HR-TEM of nano-CeO_2 with different morphologies (a, b: CeO_2-r; c, d: CeO_2-c; e, f: CeO_2-p; g: CeO_2-b)

3.5 X-ray photoelectron spectroscopy

The Ce 3d and O 1s X-ray photoelectron spectroscopy spectra of the as-prepared samples are given in Fig. 6(a). The six characteristic bands of Ce^{4+} can be clearly identified. The BE states of u''' (916.9 ± 0.1 eV) and v''' (898.3 ± 0.1 eV) are the result of the Ce $3d^9 4f^0$ O $2p^6$ final state. The lowest BE states of u'', v'', u, and v are located at 907.3, 888.5, 901.3, and 882.7 ± 0.1 eV; these states are results of Ce $3d^9 4f^1$ O $2p^5$ and Ce $3d^9 4f^2$ O $2p^4$ [30]. No obvious bands corresponding to the Ce^{3+} states could be indexed, thereby indicating that the surfaces were almost complete oxidized over all the investigated samples or that the amount of Ce^{3+} is very low but similar in the four types of ceria [31]. By the deconvolution method, the O 1s core level peak in CeO_2 could be indexed to three bands. The BE in 529.3–529.5 eV could be assigned to lattice oxygen (O_{latt}) [15, 32], whereas the BE in 531.0–531.4 eV is ascribed to surface-adsorbed oxygen (O_{ads}) [15, 32, 33]. The high BE in 533.0–533.5 eV is attributed to the surface hydroxyl species and/or adsorbed water [32-34]. The ratios of each surface oxygen species were calculated, and the results are listed in Table 2. This table shows that the amount of oxygen species was significantly different for all investigated samples. The order of adsorbed oxygen species was CeO_2-r > CeO_2-b > CeO_2-p > CeO_2-c. Surface adsorbed oxygen species are known to have high mobility and usually regarded as active oxygen species in CVOC combustion [33, 35, 36]. This could explain the high performance of CeO_2-r in DCM oxidation. The activity of the investigated samples was basically consistent with the amount of absorbed oxygen species on their surface (Fig. 1).

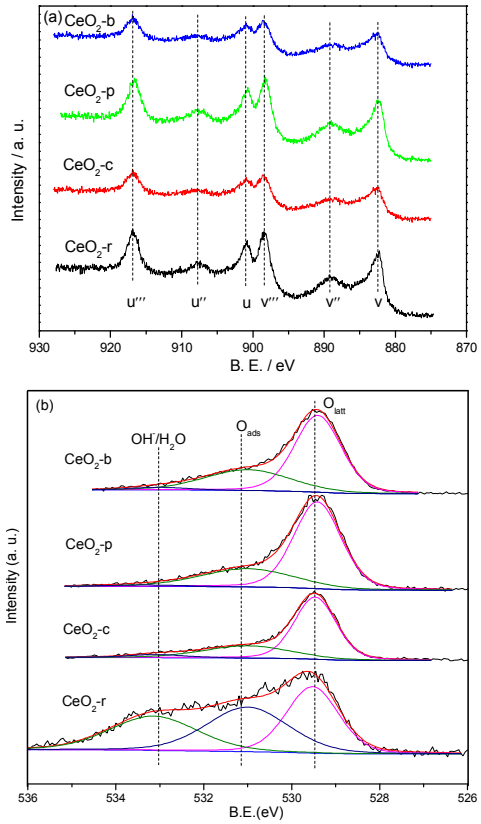

Fig. 6 XPS profiles of CeO_2 with different morphologies: Ce 3d (a) and O 1s (b).

View Article Online
DOI: 10.1039/C6RA14699F

Table 2 Amount of each surface oxygen species

Samples	Lattice oxygen		Adsorbed oxygen		OH^- and/or H_2O	
	%	BE (eV)	%	BE (eV)	%	BE (eV)
CeO_2-r	34.3	529.5	36.1	531.0	29.7	533.1
CeO_2-c	67.3	529.5	28.0	531.0	4.7	533.1
CeO_2-p	69.3	529.4	28.9	531.0	1.8	533.3
CeO_2-b	65.1	529.4	32.2	531.0	2.7	533.0

3.6 Raman spectroscopy results

Raman spectroscopy, known to be highly sensitive for detecting the concentrations of the oxygen vacancies of CeO_2, was performed here for CeO_2 with anisotropic shapes. As shown in Fig. 7, a strong band in about 463 cm^{-1} and a weak band in about 598 cm^{-1} were clearly observed on all samples, which could be indexed to the F_{2g} and defect-induced (D) models of cubic CeO_2 fluorite phase[20, 31], respectively. Also the relative intensity ratio of I_D (598 cm^{-1})/I_{F2g} (463 cm^{-1}) was used to estimate the defect concentration on CeO_2, and results were listed in Table 1. The I_D/I_{F2g} ratio of all tested samples followed the order CeO_2-r > CeO_2-b > CeO_2-p > CeO_2-c, indicating that the CeO_2-r have more defect concentrations than the others. The results were also consistent with their activity in DCM oxidation.

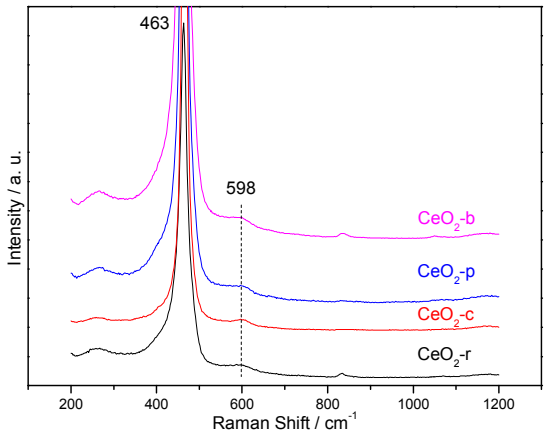

Fig. 7 Raman spectra of CeO_2 with different morphologies

4 Stability test of CeO_2 nanorods in DCM oxidation

Since CeO_2-r was highly active in DCM oxidation among all investigated samples, the stability of this sample in DCM oxidation was investigated in 325 °C for 100 h continuous testing, the result is shown in Fig. 8. It could be observed that CeO_2-r experienced a slowly deactivation in the initial 7 h testing, then stabilized. The conversion of DCM could be maintained at 83%–85% hereafter. The initial deactivation of CeO_2-r could be attributed to the adsorption of chlorine species on the surface of CeO_2 as discussed above.

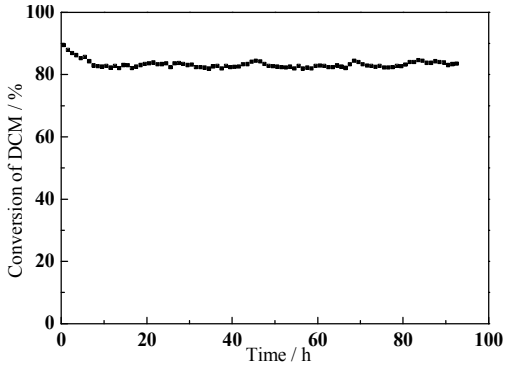

Fig. 8 Stability test of CeO_2-r in DCM oxidation at 325 °C (1000 ppm DCM, air balance, GHSV: 15000 mL · g_{cat}^{-1} · h^{-1})

5 Discussion

CeO_2 nanorods, nanocubes, and nanopolyhedra were well synthesized by a facile hydrothermal method. Using DCM oxidation as a model reaction, the morphology-dependent properties of CeO_2 nano-catalysts were investigated. CeO_2 nanorods showed much higher activity and better selectivity than CeO_2 nanocubes, CeO_2 nanopolyhedra and bulk CeO_2 nanoparticles in DCM oxidation. XRD results showed that the four synthesized samples exhibited cubic fluorite CeO_2 crystallite phase with different crystallite sizes. No other crystallite phases can be identified. The discrepancies of the tested activity with their crystallite sizes, BET surface areas, total pore volume, and pore sizes imply that the morphologies properties of ceria may play important roles in DCM oxidation. H_2-TPR results showed the reducibility and H_2 consumption of CeO_2 followed the order: CeO_2-r > CeO_2-b > CeO_2-p > CeO_2-c, which is mainly consistent with their activity in DCM oxidation. HR-TEM showed that CeO_2 nanorods selectively exposed {1 1 0} and {1 1 1} planes, CeO_2 nanocubes selectively exposed {1 0 0}, {1 1 0} planes, and CeO_2 nanopolyhedra selectively exposed {1 1 1} planes, while the bulk CeO_2 nanoparticles presented undifferentiated shapes. It is well known that the CeO_2 {1 1 0} planes and {1 1 1} planes are both nonpolar surfaces composed with stoichiometric Ce^{4+} and O atoms, while the {1 0 0} surfaces of CeO_2 are polar planes with O atom layers terminated [20]. The nonpolar {1 1 0} and {1 1 1} surfaces may benefit the adsorption of DCM with nonpolar properties. Given the deconvolution of O 1s core level spectra, the amount of adsorbed oxygen species on the surface of CeO_2 followed the order: CeO_2-r > CeO_2-b > CeO_2-p > CeO_2-c. It is generally accepted that the adsorbed oxygen species are active in CVOC destruction; thus, the activity of ceria with anisotropic shapes was mainly consistent with the order of their adsorbed oxygen species. Generally, the adsorbed oxygen species are usually related to oxygen vacancies on the surface of CeO_2. Raman spectra showed the defect concentration on CeO_2 also followed the order: CeO_2-r > CeO_2-b > CeO_2-p > CeO_2-c. Since the {1 1 0} surfaces are more exposed Ce cations than the {1 0 0} and {1 1 1} surfaces, the electrostatic interactions between the adsorbed oxygen species and Ce cations are stronger on CeO_2 nanorods than on CeO_2 nanocubes and CeO_2 nanopolyhedra; thus, it is rational that the stability and amount of adsorbed oxygen species on the CeO_2 {1 1 0} plane are more than those on the {1 0 0} and {1 1 1}

View Article Online
DOI: 10.1039/C6RA14699F

planes. The results are also consistent with the order of oxygen vacancy formation energy of CeO_2 surfaces: {1 1 0} < {1 0 0} < {1 1 1}, as demonstrated by DFT calculations [20, 24, 31]. Therefore, CeO_2 nanorods showed better performance in DCM destruction than the CeO_2 nanocubes, CeO_2 nanopolyhedra, even bulk CeO_2 nanoparticles.

6 Conclusions

CeO_2 nanorods, nanocubes, and nanopolyhedra and bulk CeO_2 nanoparticles were well synthesized and used in DCM destruction. Characterization revealed that CeO_2 nanorods selectively exposed {1 1 0} and {1 1 1} planes with better reducibility, as well as more surface adsorbed oxygen species and oxygen vacancies concentration than the other samples. Therefore, CeO_2 nanorods showed the best activity and good stability during long-term testing in DCM oxidation.

Acknowledgement

The authors thank the financial support of Natural Science Foundation of China (No. 21107096).

Notes and references

[1] S. Ojala, S. Pitkaaho, T. Laitinen, N.N. Koivikko, R. Brahmi, J. Gaalova, L. Matejova, A. Kucherov, S. Paivarinta, C. Hirschmann, T. Nevanpera, M. Riihimaki, M. Pirila, R.L. Keiski, Top. Catal. 54 (2011) 1224-1256.
[2] P. Yang, S. Yang, Z. Shi, Z. Meng, R. Zhou, Appl. Catal. B 162 (2015) 227-235.
[3] I. Maupin, L. Pinard, J. Mijoin, P. Magnoux, J. Catal. 291 (2012) 104-109.
[4] S. Pitkäaho, L. Matejova, S. Ojala, J. Gaalova, R.L. Keiski, Appl. Catal. B 113–114 (2012) 150-159.
[5] L. Jin, R. Ma, J. Lin, L. Meng, Y. Wang, M. Luo, Ind. Eng. Chem. Res. 50 (2011) 10878-10882.
[6] X. Zhang, Z. Pei, X. Ning, H. Lu, H. Huang, RSC ADVANCES 5 (2015) 79192-79199.
[7] M. Romero-Sáez, D. Divakar, A. Aranzabal, J.R. González-Velasco, J.A. González-Marcos, Appl. Catal. B 180 (2016) 210-218.
[8] A. Aranzabal, M. Romero-Saez, U. Elizundia, J.R. Gonzalez-Velasco, J.A. Gonzalez-Marcos, J. Catal. 296 (2012) 165-174.
[9] R.W. van den Brink, P. Mulder, R. Louw, Catal. Today 54 (1999) 101-106.
[10] V. de Jong, M.K. Cieplik, W.A. Reints, F. Fernandez-Reino, R. Louw, J. Catal. 211 (2002) 355-365.
[11] W. Cen, Y. Liu, Z. Wu, J. Liu, H. Wang, X. Weng, J. Phys. Chem. C 118 (2014) 6758-6766.
[12] Q. Dai, X. Wang, G. Lu, Appl. Catal. B 81 (2008) 192-202.
[13] X.Y. Wang, Q. Kang, D. Li, Catal. Commun. 9 (2008) 2158-2162.
[14] B. de Rivas, R. Lopez-Fonseca, C. Sampedro, J.I. Gutierez-Ortiz, Appl. Catal. B 90 (2009) 545-555.
[15] H. Huang, Y. Gu, J. Zhao, X. Wang, J. Catal. 326 (2015) 54-68.
[16] Y. Li, W. Shen, Chem. Soc. Rev. 43 (2014) 1543-1574.
[17] K. Deori, C. Kalita, S. Deka, J. Mater. Chem. A 3 (2015) 6909-6920.
[18] Y. Li, Z. Wei, F. Gao, L. Kovarik, C.H.F. Peden, Y. Wang, J. Catal. 315 (2014) 15-24.
[19] M. Li, Z. Wu, S.H. Overbury, J. Catal. 306 (2013) 164-176.
[20] Y. Gao, W. Wang, S. Chang, W. Huang, Chem. Cat. Chem. 5 (2013) 3610-3620.
[21] Tana, M. Zhang, J. Li, H. Li, Y. Li, W. Shen, Catal. Today 148 (2009) 179-183.
[22] Z. Hu, X. Liu, D. Meng, Y. Guo, Y. Guo, G. Lu, ACS Catal. (2016) 2265-2279.
[23] W. Han, W. Wen, J.C. Hanson, X. Teng, N. Marinkovic, J.A. Rodriguez, J. Phys. Chem. C 113 (2009) 21949-21955.
[24] R. Si, M. Flytzani-Stephanopoulos, Angew. Chem. Int. Ed. 47 (2008) 2884-2887.
[25] H. Mai, L. Sun, Y. Zhang, R. Si, W. Feng, H. Zhang, H. Liu, C. Yan, J. Phys. Chem. B 109 (2005) 24380-24385.
[26] Q.G. Dai, X.Y. Wang, G.Z. Lu, Appl. Catal. B 81 (2008) 192-202.
[27] B. de Rivas, C. Sampedro, R. Lopez-Fonseca, M.A. Gutierrez-Ortiz, J.I. Gutierrez-Ortiz, Appl. Catal. A 417 (2012) 93-101.
[28] W. Mišta, M.A. Małecka, L. Kępiński, Appl. Catal. A: General 368 (2009) 71-78.
[29] H.C. Yao, Y.F.Y. Yao, J. Catal. 86 (1984) 254-265.
[30] E. Beche, P. Charvin, D. Perarnau, S. Abanades, G. Flamant, Surf. Interface Anal. 40 (2008) 264-267.
[31] Z. Wu, M. Li, J. Howe, H.M. Meyer, S.H. Overbury, Langmuir 26 (2010) 16595-16606.
[32] P. Yang, Z. Meng, S. Yang, Z. Shi, R. Zhou, J. Mol. Catal. A 393 (2014) 75-83.
[33] Q. Dai, S. Bai, Z. Wang, X. Wang, G. Lu, Appl. Catal. B 126 (2012) 64-75.
[34] K. Sutthiumporn, S. Kawi, Int. J. Hydrogen Energy 36 (2011) 14435-14446.
[35] P. Zhao, C. Wang, F. He, S. Liu, RSC Advances 4 (2014) 45665-45672.
[36] Q. Dai, S. Bai, H. Li, W. Liu, X. Wang, G. Lu, Appl. Catal. B 168–169 (2015) 141-155.

View Article Online
DOI: 10.1039/C6RA14699F

Morphology-dependent properties of CeO_2 nano-catalysts on CH_2Cl_2 oxidation: A diagrammatic drawing of dichloromethane oxidation over CeO_2 nanorods, Xinhua Zhang, Zhiying Pei, Hanfeng Lu, Haifeng Huang, RSC Advances.